



This is a repository copy of *On the use of cryomilling and spark plasma sintering to achieve high strength in a magnesium alloy.*

White Rose Research Online URL for this paper:  
<http://eprints.whiterose.ac.uk/103342/>

Version: Accepted Version

---

**Article:**

Guan, D., Rainforth, W.M. [orcid.org/0000-0003-3898-0318](https://orcid.org/0000-0003-3898-0318), Sharp, J. et al. (2 more authors) (2016) On the use of cryomilling and spark plasma sintering to achieve high strength in a magnesium alloy. *Journal of Alloys and Compounds*, 688. pp. 1141-1150. ISSN 0925-8388

<https://doi.org/10.1016/j.jallcom.2016.07.162>

---

**Reuse**

This article is distributed under the terms of the Creative Commons Attribution-NonCommercial-NoDerivs (CC BY-NC-ND) licence. This licence only allows you to download this work and share it with others as long as you credit the authors, but you can't change the article in any way or use it commercially. More information and the full terms of the licence here: <https://creativecommons.org/licenses/>

**Takedown**

If you consider content in White Rose Research Online to be in breach of UK law, please notify us by emailing [eprints@whiterose.ac.uk](mailto:eprints@whiterose.ac.uk) including the URL of the record and the reason for the withdrawal request.



[eprints@whiterose.ac.uk](mailto:eprints@whiterose.ac.uk)  
<https://eprints.whiterose.ac.uk/>

# Accepted Manuscript

On the use of cryomilling and spark plasma sintering to achieve high strength in a magnesium alloy

Dikai Guan, W. Mark Rainforth, Joanne Sharp, Junheng Gao, Iain Todd



PII: S0925-8388(16)32196-X

DOI: [10.1016/j.jallcom.2016.07.162](https://doi.org/10.1016/j.jallcom.2016.07.162)

Reference: JALCOM 38331

To appear in: *Journal of Alloys and Compounds*

Received Date: 31 March 2016

Revised Date: 14 July 2016

Accepted Date: 16 July 2016

Please cite this article as: D. Guan, W.M. Rainforth, J. Sharp, J. Gao, I. Todd, On the use of cryomilling and spark plasma sintering to achieve high strength in a magnesium alloy, *Journal of Alloys and Compounds* (2016), doi: 10.1016/j.jallcom.2016.07.162.

This is a PDF file of an unedited manuscript that has been accepted for publication. As a service to our customers we are providing this early version of the manuscript. The manuscript will undergo copyediting, typesetting, and review of the resulting proof before it is published in its final form. Please note that during the production process errors may be discovered which could affect the content, and all legal disclaimers that apply to the journal pertain.

# On the use of cryomilling and spark plasma sintering to achieve high strength in a magnesium alloy

Dikai Guan, W. Mark Rainforth\*, Joanne Sharp, Junheng Gao, Iain Todd

*Department of Materials Science and Engineering, University of Sheffield, Sheffield S1 3JD, UK*

\*Corresponding author: *Department of Materials Science and Engineering, University of Sheffield, Sheffield S1 3JD, UK*

*Email address: m.rainforth@sheffield.ac.uk*

**Abstract:** Bulk nanostructured magnesium alloy AZ31 has been produced by spark plasma sintering at four different temperatures from 350 to 450 °C. The effect of sintering temperature on microstructural evolution and compression behaviour was studied in detail. It was concluded that the sample consolidated at 400 °C exhibited the highest strength. Higher sintering temperature (450 °C) improved the compressive strain of the bulk sample but at the sacrifice of strength. However, samples consolidated at 350 °C displayed brittle behaviour with low strength. All consolidated samples had a bimodal microstructure with nanocrystalline and coarse grains. The nanocrystalline microstructure formed by cryomilling was retained after consolidation and a maximum microhardness was approximately 150 HV. The bulk samples consolidated at 400 °C with an average grain size of 45 nm showed exceptional average true compressive yield strength of 400.7 MPa, true ultimate compressive strength of 499.7 MPa, which was superior to published results for most of conventional magnesium alloys. Although nanostructured materials usually have high strength but poor ductility, the material in this study exhibited high strength and a true compressive strain of 0.036.

**Keywords:** Magnesium alloy; Cryomilling; Spark plasma sintering; Hall-Petch effect; Grain refinement

## 1 Introduction

Magnesium has low density and a high specific stiffness and strength, and is therefore an outstanding candidate for weight critical structural applications [1]. However, the low ductility and relatively poor mechanical strength compared to most light aluminium alloys limit the applications of magnesium alloys [2]. Grain refinement is a very effective route to improve the strength and ductility as a result of the Hall-Petch effect [3]. This is particularly true for magnesium, having a hexagonal close packed structure, which exhibits a higher Hall-Petch coefficient ( $k_y$ ) than face centred cubic metals, such as aluminium (magnesium:  $k_y=279$  MPa  $\mu\text{m}^{-1/2}$  and aluminium:  $k_y=68$  MPa  $\mu\text{m}^{-1/2}$ ) [4].

Grain refinement is an effective way to achieve high strength magnesium alloys and advanced processing methods to achieve this goal were reviewed by Pan et al. [5]. To produce magnesium alloys with ultrafine-grained or even nanocrystalline microstructure, severe plastic deformation (e.g. equal channel angular pressing, high-pressure torsion, multi-directional forging and mechanical milling) has been applied to magnesium alloys [5-15]. For example, a Mg-1.78Zn-0.89Mn alloy with average grain size of 700 nm was produced via two-step equal channel angular pressing process [16].

Recently, Kim et al. [17, 18] reported an exceptionally strong AZ31 alloy produced by high-ratio differential speed rolling that resulted in an ultrafine-grained structure (average grain size of 0.6  $\mu\text{m}$ ) giving a yield stress of 382 MPa. Razavia et al. [15] reported that the grain size of AZ31 produced by ECAP could be reduced to 350 nm, giving an alloy with a yield strength of 385 MPa and ultimate tensile strength of 455 MPa with 13% ductility, which is the highest reported combined strength and ductility for an AZ31 alloy. Meng, Lu, Trividly and co-authors [19-21] found that an ultrafine-grained or nanocrystalline microstructure could be obtained in precipitate-hardened magnesium alloys via severe plastic deformation processes due to the combined high deformation and significant pinning effect from precipitates. With addition of 0.46% CaO, the strength of ultrafine-grained AZ31-CaO produced by 6 passes of equal channel angular pressing was enhanced without the loss of ductility [22]. Furthermore, Lee, Morisada and co-authors [23, 24] found that an ultrafine-grained or nanocrystalline microstructure could be obtained in Mg-based composites via friction stir processing due to effective pinning effect from reinforcing particles. In contrast, for low alloy content, such as in commercially pure magnesium and alloys such as AZ31, it is a challenge to achieve even an ultrafine-grained microstructure, let alone a nanocrystalline

structure due to the rapid growth kinetics of the single-phase grains. Nevertheless, Chang et al. [25] reported that they managed to produce a nano-grained microstructure in AZ31 alloy with an average grain size of 85 nm by using two-pass friction stir processing with rapid heat sink [26]. The mean hardness of this alloy was around 150 HV, but other mechanical properties were not included in their published papers. In addition, Sun et al. [27] reported a nanocrystalline bulk AZ31 with an average grain size of 48 nm by powder metallurgy assisted hydriding–dehydriding and its hardness was about 89 HV, but again no resulting mechanical properties was reported. Most recently, Zhou et al. [28] produced a nanocrystalline AZ31 magnesium alloy via mechanical milling and cold pressing. The average grain size was refined to 66-86 nm by adding various amounts of titanium particles and producing a hardness of 147 HV and yield strength and 293 MPa at room temperature.

A novel manufacturing technology that comprises a combination of cryomilling and spark plasma sintering has recently been successfully applied to fabricate nanocrystalline Mg-30Al and AZ80 alloys [29-32]. The nanocrystalline AZ80 exhibited an excellent compressive yield stress of 442 MPa and ultimate compressive strength of 546 MPa with an average compressive strain to failure of 3.7%. The nanocrystalline Mg-10Al exhibited a remarkable ultimate compressive strength of 579.7 MPa with a compressive strain to failure of 2.4%. The retained nanocrystalline reported in these papers can be also partly attributed to the rapid sintering process by using spark plasma sintering. In addition, nanostructured magnesium composites were also produced by cryomilling and spark plasma sintering that exhibited excellent thermal stability [33, 34]. The yield strength was 330 MPa in Mg-10Al-1diamantane even after 100 h of annealing at 400 °C [33].

The motivations of the current study are twofold. Firstly, to find out whether this novel manufacturing technology can be extended to produce nanocrystalline in a magnesium AZ31 alloy with much lower alloying content than Mg-30Al and AZ80 alloys, thereby fabricating high strength nanocrystalline AZ31 alloy. Secondly, to investigate the response of grain growth and mechanical behaviour when samples were sintered at various temperatures, especially at elevated temperatures (e.g., 450 °C, 0.78 Tm).

## **2 Experimental**

### **2.1 Cryomilling of magnesium alloy AZ31**

The as-received powder used in this study was 200 mesh ( $-75\ \mu\text{m}$ ) helium gas atomized AZ31 powder (Magnesium Elektron Ltd, USA) and particle size between  $38\text{-}75\ \mu\text{m}$  was sieved and used for cryomilling and spark plasma sintering. 6 grams of powder and a stainless steel  $\varnothing 25\ \text{mm}$  grinding ball were loaded into a sealed grinding jar in an argon glovebox (MBraun, Germany) to avoid oxidation. The cryomilling was performed using a cryomill (Retsch, Germany) with an integrated cooling system. Liquid nitrogen circulated through the system and was continually replenished from an autofill system to keep the temperature at  $-196\ ^\circ\text{C}$  and avoid direct contact with liquid nitrogen. There was no evidence that the nitrogen reacted in any way with the powder. The shaking frequency of the grinding balls was 22 Hz and the cryomilling time was 6 hours (designated as CM6h powder).

## 2.2 Spark plasma sintering of bulk nanostructured magnesium alloy AZ31

3 grams of cryomilled powder was loaded into a cylindrical graphite die with diameter of 20 mm. To avoid welding and obtain a more uniform current flow, thin graphite foils were placed between powders and the graphite dies surface. The prepressed powder was then sintered by spark plasma sintering (FCT Systeme GmbH spark plasma sintering system, type HP D 1050, Germany) under vacuum. A heating rate of  $50^\circ\text{C}/\text{min}$  followed by a dwell time 5 minutes with a maximum uniaxial pressure of 80 MPa were applied for sintering based on the results of preliminary experiments. The holding temperatures ranged from 350 to  $450^\circ\text{C}$ . The corresponding sintered samples were designated CM350, CM400 and CM450 hereafter (Table 1). The temperature was monitored by a TC thermocouple inserted into a hole located in the centre of the die close to the sample. To provide a base-line to compare the cryomilled powders, the as-received powder (diameter in the range  $38\text{-}75\ \mu\text{m}$ ) was sintered at  $400\ ^\circ\text{C}$ , designated as AR400 (Table 1). In order to avoid oxidation, the powders were loaded into the grinding jar before cryomilling and the spark plasma sintering mould in an argon atmosphere glove box (Mbraun, Germany). The current, temperature, displacement and displacement rate as a function of time were recorded by the software equipped with the spark plasma sintering apparatus.

## 2.3 Density measurement

After polishing the surface, the bulk density of the sintered samples was determined by the Archimedes method using a balance with accuracy of  $\pm 0.0001\ \text{g}$  (MS104S, Mettler Toledo, Switzerland). At least three measurements were taken for each sample.

## 2.4 Microstructure characterisation

A Siemens X-Ray Diffractometer D5000 using Cu K $\alpha$  ( $\lambda = 0.15406$  nm) radiation was employed to study the crystallite size of cryomilled powders. The diffractometer has a programmable divergence slit with a 0.02 rad Soller and a 1 degree divergence slit on the Cu K $\alpha$  x-ray source. The detector was set to read from 30° to 80° at 2.4 s/step with a step size of 0.02°. 10 grams of as-received AZ31 powder was annealed at 450 °C for 8 hours in a vacuum furnace. This fully annealed as-received AZ31 powder was used as a standard to subtract instrumental broadening. XRD peak profiles were fitted by Pearson VII function, and full width at half maximum was used as a measure of peak broadening. The pure sample peak broadening  $B$  was calculated using  $B = \sqrt{B_{obs}^2 - B_{inst}^2}$ , where  $B_{obs}$  is the observed peak broadening, and  $B_{inst}$  is the instrumental broadening. Samples for optical microscopy and scanning electron microscopy (SEM) were prepared by grinding with SiC paper from 1200 to 4000 grit. To minimise oxidation through exposure to water, samples were polished with alcohol based diamond suspensions of 1 and 0.25 $\mu$ m. Some samples for grain size measurement were etched using an acetic-picric solution (4.2g picric acid, 10ml acetic acid, 70ml ethanol and 10ml water) for 1 s. Transmission electron microscopy (TEM) samples of cryomilled powder were prepared by grinding using a mortar and pestle and suspended in isopropanol, followed by ultrasonic dispersion and then deposition onto a 200 mesh Cu grid with holey carbon film. Thin foils of bulk samples were prepared by the combination of grinding, dimpling and ion milling.

## 2.5 Mechanical tests

Hardness tests were conducted using a Vickers indenter with a 50 gf load for 15 s. Fig. 1 shows the loading force direction and also cube specimens' sizes for compression tests. Prior to testing, all the samples were carefully polished to eliminate oxide layers attached on each surface. Compression tests were conducted using a Zwick/Roell universal testing machine at a crosshead speed of 0.06 mm/min until failure. All experimental data has been corrected for machine compliance [35].

# 3 Results and discussion

## 3.1 Cryomilled Powder of Magnesium Alloy AZ31

### 3.1.1 Particle size and morphology

Fig. 2(a) shows particle size and morphology of the as-received gas atomized AZ31 powder. Fig. 2(b) shows the grain structure, with an average grain size of  $2.03 \pm 0.47 \mu\text{m}$ . Fig. 2(c) shows the particle morphology after cryomilling for 6 hours. Most of the coarse as-received particles were crushed into fine particles with an average size of  $25 \mu\text{m}$ . Fig. 2 (d) shows a deformed particle where evidence of cold welding and fracture can be clearly seen, in agreement with other published observations [32].

The evolution of particle morphology can be explained by cold welding and fracture occurring during the cryomilling process [36-39]. The grinding balls plastically deform the particles resulting in work hardening and fracture. Fresh fractured surfaces are known to promote cold welding [36], which leads to an increase particle size. However, with continued severe cold deformation, fracture becomes dominant over cold welding, resulting in a reduction in particles size. With further extended milling, cold welding and fracture reach a balance and the particle size does not change with further milling time.

### 3.1.2 Grain size

Fig. 3 shows XRD patterns of as-received and CM6h powders. Compared to the as-received powder, significant peak broadening was evident after cryomilling for 6h. Due to severe plastic deformation and very limited recovery and recrystallization during cryomilling, this peak broadening can be attributed to the ultra-fine crystallite size and high internal microstrain. Approximating the crystallite size and microstrain broadening profiles by a Cauchy function, the relationship between crystallite size ( $d$ ) and the internal microstrain  $\varepsilon$  can be fitted using Williamson-Hull plot (Equation 1):

$$B \times \cos(\theta) = \frac{K \times \lambda}{D} + 4 \times \varepsilon \times \sin(\theta) \quad (\text{Equation 1})$$

Where  $B$  is pure sample diffraction FWHM breadth as defined above,  $\theta$  is the position of peak maximum,  $K$  is a constant as 0.94,  $\lambda$  is the wavelength of the X-ray radiation (Cu, 0.154056 nm),  $D$  is the average crystallite size and  $\varepsilon$  is the microstrain. By performing a least squares fit to  $B \cos(\theta)$  against  $\sin(\theta)$  for all of the measured peaks of a sample, the average crystallite size was estimated to be 32 nm for powder sample CM6h.

After 6 hours cryomilling, the grain size was significantly refined to the nanometre scale. Fig. 4(a) shows a transmission electron microscope bright field (BF) image and selected area electron diffraction (SAED) pattern of the CM6h powder. The diffraction rings indicated that most of the grains were nano sized with a random crystal orientation. Fig. 4(b) gives the grain size distribution of the 6h cryomilled powder (determined from 200 grains measure) and its average size is  $26.2\pm 7.9$  nm, which is close to the grain size of 32 nm estimated by XRD.

Because the main difference between cryomilling and mechanical milling is the working temperature, the mechanism of nanostructure formation during cryomilling can be considered as a mechanical milling process [36]. Due to the cryogenic milling temperature, suppression of recovery in the material was significant, which plays a positive role in reducing the milling time to obtain nanocrystallites [40]. Fecht stated there are three main stages of microstructure mechanically milling process [41]. Firstly, localized deformation occurs in shear bands consisting of high density dislocation arrays; secondly, because these dislocation arrays are not stable and dislocation annihilation and recombination and annihilation of dislocations then ensues, this results in the formation of nano-sized subgrains; with further deformation, the subgrains with low angle grain boundaries (LAGB) transform to small grains with high angle grain boundaries (HAGB) by the annihilation and recombination of more dislocations into the boundaries or accompanying subgrains rotation during collision. Finally, this LAGB structure is able to change to completely random HAGB between individual grains.

## 3.2 Bulk sintered AZ31 samples

### 3.2.1 Density and morphology

The theoretical density of AZ31 alloy was calculated to be  $1.780\text{ g/cm}^3$ . Table 1 provides the density measurement results of the four samples. CM450 had the highest density of  $1.766\text{ g/cm}^3$  while CM350 had the lowest density of  $1.691\text{ g/cm}^3$ . As expected, higher sintering temperature led to increased bulk density. The distribution of pores and cracks was investigated by using optical microscopy. Fig. 5(a) shows a large-scale optical microscope (OM) image of sample AR400. Considerable porosity can clearly be observed. These pores arose from insufficient sintering and also occurred due to particle pull out during polishing

because of insufficient inter-particle bonding. In addition, a layer of magnesium oxide film was found to cover each particle, which in itself would have restricted the sintering process. Figs. 5(b-d) present the OM images of sample CM350, CM400 and CM450, respectively. The most obvious feature in these images is that the volume fraction of micro pores decreased substantially when the sintering temperature rose from 350 °C to 400 °C. The pores size and quantity slightly decreased when the sintering temperature was increased from 400 °C to 450 °C. Therefore, higher sintering temperature increased density, which was attributed to two factors. Firstly, the strength of the alloy powder drops substantially with increasing temperature. Secondly, creep flow is the main densification mechanism in the case of pressure-assisted sintering at elevated temperatures and is a diffusion-driven process which strongly relies on temperature [42].

It was evident that not all the particles in the starting powder had been reduced in size by the milling process. This led to a bimodal particle size distribution, with larger particles (which exhibited brighter contrast in Fig. 5) distributed amongst the much finer structure in all sintered cryomilled samples. The volume fraction of the larger particles in each sintered cryomilled sample was measured to be approximately 25%. This is inevitable with mechanical milling, especially without adding process control agent. The hardness of these particles that had not been reduced in size was only approximately 70 HV with a mean grain size of about 10  $\mu\text{m}$ . This fraction of coarser particles will offset the improvement in the mechanical properties from those particles containing a nanostructure, as discussed later.

Because samples AR400 and CM400 were processed under the same operating parameters, the effect of cryomilling on sample densification can be discussed. Fig. 6 shows back-scattered SEM images of AR400 and CM400 samples after sintering. Pores were observed in both sintered samples between particle boundaries (indicated by the white arrows). However, the pores were smaller and fewer in number in sample CM400 compared to sample AR400. The boundaries were difficult to find in the CM400 sample, whereas they were clear in the AR400 material. This was probably because the oxide film present on the surface of the magnesium powder had been broken up during cryomilling, such that particle boundaries could only be seen in the as-received material. The oxide films appeared to have been broken down to nano-sized inclusions and would therefore be expected to act to strengthen the alloy [43] (which is discussed in more detail in a separate publication).

The aluminium, zinc and manganese rich second phases that were apparent and locally distributed in sample AR400 were broken up and uniformly dispersed in the cryomilled sample CM400. It is also possible that the milling resulted in some dissolution of these second phases, as milling is well known to increase the equilibrium solubility of equilibrium solubility limit at room temperature and to dissolution of second phase particles [43]. These effects can also make contribution to increase the strength of the alloy [43].

Fig. 7(a) shows a typical secondary electron SEM image of sample AR400 in the as-sintered condition and Fig. 8(a) gives the grain size distribution of all samples measured from such SEM images. This suggested an average grain size of 6.5  $\mu\text{m}$  for sample AR400, which is larger than in the as-received powder. Interestingly, the grain size adjacent to the magnesium oxides rich was finer, Fig. 7(a), which suggested that the oxide film locally pinned the grain boundaries.

Figs. 7(b,c,d) give bright field TEM images of samples CM350, CM400 and CM450. The corresponding grain size distributions in the nanocrystalline areas, obtained by TEM, are given in Figs. 8 (b,c,d), which yielded average grain sizes in the nanocrystalline area of 35nm, 45nm and 60 nm. Note that this size distribution does not include the ~25% fraction of particles which retained a coarse grain size after cryomilling. Fig. 9 shows a region of bimodal grain structure taken from the CM400.

SEM images, such as the one in Fig. 7 (a) showed that the original particle boundaries were decorated by what was presumed to be a magnesium oxide film that covered the surface of the as-received powder during cryomilling. These oxides were further investigated using TEM. Fig. 7(a) shows high angle annular dark field (HAADF) image of the bulk CM400 sample, which clearly demonstrates some lower atomic number (dark contrast) particles were located at a grain boundary. Electron energy loss spectroscopy (EELS) was used to investigate possible phases at the grain boundary. Fig. 10 (b) shows the EELS image collected from red point in Fig. 10 (a) and Fig. 10 (c) shows a reference spectrum of magnesium oxides from Gatan EELS Atlas. The presence of oxygen was confirmed by the spectrum. The shape of the ionisation edges, which is a signature of the phase, exhibited a good match between our results, Fig. 10 (b), and the reference standard for MgO, Fig. 10 (c). These oxide particles were fine and distributed as discrete particles embedded in the grain boundaries, which therefore would have been expected to act as pinning sites.

### 3.2.2 Micro hardness results of bulk samples produced by spark plasma sintering

Fig. 11 gives the hardness results of bulk samples processed from 350 °C to 450 °C. The hardness of the bulk AR400 sample was only  $70\pm 5.6$  HV. In contrast, the hardness of samples CM350 and CM400 increased significantly to approximately 150HV after cryomilling, resulting in a material with hardness more than twice that of bulk AR400 sample. However, when the sintering temperature was further increased to 450°C, the hardness was lower at around 135 HV.

### 3.2.3 Compression testing behaviour

Fig. 12 gives true compressive stress-strain curves of samples AR400, CM350, CM400 and CM450. The corresponding compressive properties are listed in Table 1. To illustrate the influence of cryomilling and sintering temperature on bulk materials, the following section will first focus on the reasons for the exceptional high strength with poor ductility material derived from cryomilled powder, and the mechanical behavior response on various sintering temperatures will be discussed afterwards.

The measured average true ultimate compressive strength and yield strength (0.2% proof stress) of the cryomilled sample CM400 was 499.7 MPa and 400.7 MPa, respectively. These values were significantly higher compared to the sample produced from the as-received powder, AR400, with a true ultimate compressive strength of 357.6 MPa and a yield strength of 180.5 MPa. Moreover, these values also exceed the previously reported highest yield strength of 385 MPa and ultimate strength of 455 MPa in AZ31 alloy [15].

The average true compressive strain of sample CM400 (measured at the ultimate true compressive strength) was only 3.6%, which was only about 1/3 of the bulk as-received sample and about 1/3 the result reported by Razavi et al. [15]. However, this value is still acceptable in the field of nanostructured magnesium alloys. High strength and poor ductility is prevalent in all nanostructured materials [44]. One source of poor ductility is that defects introduced from the processing, such as porosity and cracks (see Figs. 5-6), lead to low ductility [45,46]. In addition, work hardening is a key factor in determining the ductility of

nanocrystalline materials [47]. As shown in Fig. 12, extensive work hardening was observed in bulk AR400 samples, while only limited work hardening occurred in the cryomilled samples. The limited of work hardening in nanocrystalline materials can be explained by the lack of dislocation accumulation within the nanosized grains. In addition, the effect of twinning is also important. Fig. 13 presents optical microscope images of AR400 and CM400 after compression testing. Far more deformation twins were produced during compression tests for samples AR400 compared to CM400, where only one twin was observed in the coarse grained regions. Furthermore, Fig. 9 shows a bright field TEM image with bimodal microstructure, and no sign of twinning was observed. This contrasts reports of twinning in other nanostructured magnesium alloys with higher alloying contents [29, 48, 49]. The stress required for twin nucleation increases substantially with reducing grain size to the nanometre scale, thereby reducing the occurrence of twinning as grain size is reduced [45]. One influence of twinning on the plastic deformation is that unfavourably oriented grains can be adjusted into a more favourable orientation by twinning. This positive effect has been used to improve the ductility of nano-twinned Cu [50].

It would be expected that the yield strength (Fig. 12 and Table 2) would correlate with the grain size in the samples, which was a function of the sintering temperature. The histograms of grain size distribution were given in Fig. 8. The average grain size of sample CM350 was approximately ~33 nm, which was smaller than that of sample CM400 (~45 nm), and CM450 (~60 nm). It would be expected that the yield strength would scale with the grain size. This appears to be true for a comparison of CM400 and CM450, but does not hold true for CM350. However, there are additional factors that must be taken into account. Firstly, CM350 had a lower density, table 1, and this probably contributed to the limited mechanical properties. Secondly, all cryomilled samples contained a fraction (~25%) of particles that had a coarser grain size as a result of incomplete cryomilling. These will have certainly contributed to the strength, reducing the beneficial effect of the nanoscale grains. Thirdly, the fine MgO particles will have contributed to the mechanical properties, on the one hand potentially increasing work hardening rate, but at the same time acting to limit the ductility. Clearly, separating these separate contributions would be very difficult.

## 4 Conclusions

A nanocrystalline AZ31 alloy with exceptionally high strength was fabricated by a combination of cryomilling and spark plasma sintering. All the bulk samples consolidated from cryomilled powders exhibited a bimodal microstructure. The optimum conditions were obtained at a sintering temperature of 400 °C, which provided a balance between achieving full densification and minimising grain growth during sintering. This provided the highest average yield strength of 400.7 MPa and ultimate strength of 499.7 MPa with acceptable compressive true strain of 0.036. The mean grain size of the material cryomilled for 6h followed by sintering at 400°C was about 45 nm. The high strength of the sample was mainly attributed to the grain refinement strengthening, oxide dispersion and solid solution strengthening. The low compressive strain of this alloy is due to limited work hardening and pores located between particle boundaries. A higher sintering temperature of 450 °C improved compressive strain of the consolidated sample at the sacrifice of strength, whereas samples sintered at 350 °C displayed brittle behaviour with low strength. Generally, nanostructure materials usually have high strength but poor ductility.

## Acknowledgements

This work was supported by the University of Sheffield and CSC (China Scholarship Council).

## References

- [1] S.R. Agnew, J.F. Nie, Preface to the viewpoint set on: The current state of magnesium alloy science and technology, *Scr. Mater.* 63 (2010) 671-673.
- [2] H.E. Friedrich, B.L. Mordike, *Magnesium Technology: Metallurgy, Design Data, Applications*, Springer, New York, 2010.
- [3] E.O. Hall, The Deformation and Ageing of Mild Steel: III Discussion of Results, "*Proc. Phys. Soc. London, Sect. B* " 64 (1951) 747.
- [4] T.H. Courtney, *Mechanical Behavior of Materials*, Second ed., McGraw-Hill Higher Education, Boston, 2000.
- [5] H. Pan, Y. Ren, H. Fu, H. Zhao, L. Wang, X. Meng, G. Qin, Recent developments in rare-earth free wrought magnesium alloys having high strength: A review, *J. Alloys Compd.* 663 (2016) 321-331.
- [6] S. Biswas, S. Suwas, Evolution of sub-micron grain size and weak texture in magnesium alloy Mg–3Al–0.4Mn by a modified multi-axial forging process, *Scr. Mater.* 66 (2012) 89-92.

- [7] S.X. Ding, W.T. Lee, C.P. Chang, L.W. Chang, P.W. Kao, Improvement of strength of magnesium alloy processed by equal channel angular extrusion, *Scr. Mater.* 59 (2008) 1006-1009.
- [8] R.B. Figueiredo, T.G. Langdon, Development of structural heterogeneities in a magnesium alloy processed by high-pressure torsion, *Mater. Sci. Eng. A* 528 (2011) 4500-4506.
- [9] M. Furui, H. Kitamura, H. Anada, T.G. Langdon, Influence of preliminary extrusion conditions on the superplastic properties of a magnesium alloy processed by ECAP, *Acta Mater.* 55 (2007) 1083-1091.
- [10] M. Kai, Z. Horita, T.G. Langdon, Developing grain refinement and superplasticity in a magnesium alloy processed by high-pressure torsion, *Mater. Sci. Eng. A* 488 (2008) 117-124.
- [11] H. Miura, G. Yu, X. Yang, Multi-directional forging of AZ61Mg alloy under decreasing temperature conditions and improvement of its mechanical properties, *Mater. Sci. Eng. A* 528 (2011) 6981-6992.
- [12] D. Orlov, G. Raab, T.T. Lamark, M. Popov, Y. Estrin, Improvement of mechanical properties of magnesium alloy ZK60 by integrated extrusion and equal channel angular pressing, *Acta Mater.* 59 (2011) 375-385.
- [13] P. Serre, R.B. Figueiredo, N. Gao, T.G. Langdon, Influence of strain rate on the characteristics of a magnesium alloy processed by high-pressure torsion, *Mater. Sci. Eng. A* 528 (2011) 3601-3608.
- [14] J. Xing, H. Soda, X. Yang, H. Miura, T. Sakai, Ultra-Fine Grain Development in an AZ31 Magnesium Alloy during Multi-Directional Forging under Decreasing Temperature Conditions, *Mater. Trans.* 46 (2005) 1646-1650.
- [15] S.M. Razavi, D.C. Foley, I. Karaman, K.T. Hartwig, O. Duygulu, L.J. Kecskes, S.N. Mathaudhu, V.H. Hammond, Effect of grain size on prismatic slip in Mg-3Al-1Zn alloy, *Scr. Mater.* 67 (2012) 439-442.
- [16] E. Mostaed, A. Fabrizi, D. Dellasega, F. Bonollo, M. Vedani, Microstructure, mechanical behavior and low temperature superplasticity of ECAP processed ZM21 Mg alloy, *J. Alloys Compd.* 638 (2015) 267-276.
- [17] W.J. Kim, M.J. Lee, B.H. Lee, Y.B. Park, A strategy for creating ultrafine-grained microstructure in magnesium alloy sheets, *Mater. Lett.* 64 (2010) 647-649.
- [18] W.J. Kim, Y.G. Lee, M.J. Lee, J.Y. Wang, Y.B. Park, Exceptionally high strength in Mg-3Al-1Zn alloy processed by high-ratio differential speed rolling, *Scr. Mater.* 65 (2011) 1105-1108.
- [19] F. Meng, J.M. Rosalie, A. Singh, K. Tsuchiya, Precipitation behavior of an ultra-fine grained Mg-Zn alloy processed by high-pressure torsion, *Mater. Sci. Eng. A* 644 (2015) 386-391.
- [20] F. Lu, A. Ma, J. Jiang, J. Chen, D. Song, Y. Yuan, J. Chen, D. Yang, Enhanced mechanical properties and rolling formability of fine-grained Mg-Gd-Zn-Zr alloy produced by equal-channel angular pressing, *J. Alloys Compd.* 643 (2015) 28-33.
- [21] P. Trivedi, K.C. Nune, R.D.K. Misra, S. Goel, R. Jayanthan, A. Srinivasan, Grain refinement to submicron regime in multiaxial forged Mg-2Zn-2Gd alloy and relationship to mechanical properties, *Mater. Sci. Eng. A* 668 (2016) 59-65.
- [22] S.-H. Bae, K.H. Jung, Y.-C. Shin, D.J. Yoon, M. Kawasaki, Development of mechanical properties in a CaO added AZ31 magnesium alloy processed by equal-channel angular pressing, *Mater. Charact.* 112 (2016) 105-112.
- [23] C.J. Lee, J.C. Huang, P.J. Hsieh, Mg based nano-composites fabricated by friction stir processing, *Scr. Mater.* 54 (2006) 1415-1420.
- [24] Y. Morisada, H. Fujii, T. Nagaoka, M. Fukusumi, Nanocrystallized magnesium alloy – uniform dispersion of C60 molecules, *Scr. Mater.* 55 (2006) 1067-1070.

- [25] C.I. Chang, X.H. Du, J.C. Huang, Producing nanograined microstructure in Mg–Al–Zn alloy by two-step friction stir processing, *Scr. Mater.* 59 (2008) 356–359.
- [26] C.I. Chang, X.H. Du, J.C. Huang, Achieving ultrafine grain size in Mg–Al–Zn alloy by friction stir processing, *Scr. Mater.* 57 (2007) 209–212.
- [27] H.-f. Sun, W. Fang, W.-b. Fang, Producing nanocrystalline bulk Mg–3Al–Zn alloy by powder metallurgy assisted hydriding–dehydriding, *J. Alloys Compd.* 509 (2011) 8171–8175.
- [28] H. Zhou, L. Hu, Y. Sun, H. Zhang, C. Duan, H. Yu, Synthesis of nanocrystalline AZ31 magnesium alloy with titanium addition by mechanical milling, *Mater. Charact.* 113 (2016) 108–116.
- [29] B. Zheng, O. Ertorer, Y. Li, Y. Zhou, S.N. Mathaudhu, C.Y.A. Tsao, E.J. Lavernia, High strength, nano-structured Mg-Al-Zn alloy, *Mater. Sci. Eng. A* 528 (2011) 2180–2191.
- [30] M. Pozuelo, C. Melnyk, W.H. Kao, J.-M. Yang, Cryomilling and spark plasma sintering of nanocrystalline magnesium-based alloy, *J. Mater. Res.* 26 (2011) 904–911.
- [31] M. Pozuelo, W.H. Kao, J.-M. Yang, High-resolution TEM characterization of SiC nanowires as reinforcements in a nanocrystalline Mg-matrix, *Mater. Charact.* 77 (2013) 81–88.
- [32] M. Pozuelo, Y.W. Chang, J.M. Yang, Enhanced compressive strength of an extruded nanostructured Mg–10Al alloy, *Mater. Sci. Eng. A* 594 (2014) 203–211.
- [33] Y.W. Chang, M. Pozuelo, J.M. Yang, Thermally Stable Nanostructured Magnesium Nanocomposites Reinforced by Diamantane, *JOM* 67 (2015) 2828–2833.
- [34] M. Pozuelo, Y.W. Chang, J.M. Yang, Effect of diamondoids on the microstructure and mechanical behavior of nanostructured Mg-matrix nanocomposites, *Mater. Sci. Eng. A* 633 (2015) 200–208.
- [35] S.R. Kalidindi, A. Abusafieh, E. El-Danaf, Accurate characterization of machine compliance for simple compression testing, *Exp. Mech.* 37 (1997) 210–215.
- [36] D.B. Witkin, E.J. Lavernia, Synthesis and mechanical behavior of nanostructured materials via cryomilling, *Prog. Mater. Sci.* 51 (2006) 1–60.
- [37] F. Sun, P. Rojas, A. Zúñiga, E.J. Lavernia, Nanostructure in a Ti alloy processed using a cryomilling technique, *Mater. Sci. Eng. A* 430 (2006) 90–97.
- [38] E.J. Lavernia, B.Q. Han, J.M. Schoenung, Cryomilled nanostructured materials: Processing and properties, *Mater. Sci. Eng. A* 493 (2008) 207–214.
- [39] C. Suryanarayana, Mechanical alloying and milling, *Prog. Mater. Sci.* 46 (2001) 1–184.
- [40] F. Zhou, D. Witkin, S.R. Nutt, E.J. Lavernia, Formation of nanostructure in Al produced by a low-energy ball milling at cryogenic temperature, *Mater. Sci. Eng. A* 375–377 (2004) 917–921.
- [41] H.J. Fecht, Nanostructure formation by mechanical attrition, *Nanostruct. Mater.* 6 (1995) 33–42.
- [42] D. Liu, Y. Xiong, T. Topping, Y. Zhou, C. Haines, J. Paras, D. Martin, D. Kapoor, J. Schoenung, E. Lavernia, Spark Plasma Sintering of Cryomilled Nanocrystalline Al Alloy - Part II: Influence of Processing Conditions on Densification and Properties, *Metall. Mater. Trans. A* 43 (2012) 340–350.
- [43] W.-b. Fang, W. Fang, H.-f. Sun, Preparation of high-strength Mg–3Al–Zn alloy with ultrafine-grained microstructure by powder metallurgy, *Powder Technol.* 212 (2011) 161–165.
- [44] C.C. Koch, D.G. Morris, K. Lu, A. Inoue, Ductility of nanostructured materials, *MRS Bull.* 24 (1999) 54–58.
- [45] Y.T. Zhu, X. Liao, Nanostructured metals: Retaining ductility, *Nat. Mater.* 3 (2004) 351–352.
- [46] Q. Yu, Z.-W. Shan, J. Li, X. Huang, L. Xiao, J. Sun, E. Ma, Strong crystal size effect on deformation twinning, *Nature* 463 (2010) 335–338.
- [47] L. Lu, X. Chen, X. Huang, K. Lu, Revealing the Maximum Strength in Nanotwinned Copper, *Science* 323 (2009) 607–610.

- [48] B. Zheng, Y. Li, W. Xu, Y. Zhou, S.N. Mathaudhu, Y. Zhu, E.J. Lavernia, Twinning in cryomilled nanocrystalline Mg powder, *Philos. Mag. Lett.* (2013) 1-8.
- [49] M. Pozuelo, S.N. Mathaudhu, S. Kim, B. Li, W.H. Kao, J.M. Yang, Nanotwins in nanocrystalline Mg–Al alloys: an insight from high-resolution TEM and molecular dynamics simulation, *Philos. Mag. Lett.* 93 (2013) 640-647.
- [50] C. Koch, Optimization of strength and ductility in nanocrystalline and ultrafine grained metals, *Scr. Mater.* 49 (2003) 657-662.

**Table 1.** Samples designation and density measurement results

Powder type	Sintering temperature	Sample designation	Density (g/cm <sup>3</sup> )	Relative density to AZ31
As-received (AR)	400 °C	AR400	1.730±0.004	97.2%
Cryomilled (CM)	350 °C	CM350	1.691±0.003	95.0%
Cryomilled (CM)	400 °C	CM400	1.755±0.004	98.6%
Cryomilled (CM)	450 °C	CM450	1.766±0.005	99.2%

**Table 2.** Summary of compressive properties of bulk as-received and cryomilled samples

Samples	No.	0.2% Proof Stress (MPa)	True Ultimate Strength (MPa)	True strain at ultimate strength
AR400	1	185.7	359.8	0.111
	2	175.3	355.3	0.120
CM350	1	345.2	399.8	0.019
	2	331.3	372.7	0.018
CM400	1	401.2	500.2	0.036
	2	400.2	499.2	0.036
CM450	1	394.7	478.5	0.055
	2	361.2	484.5	0.050

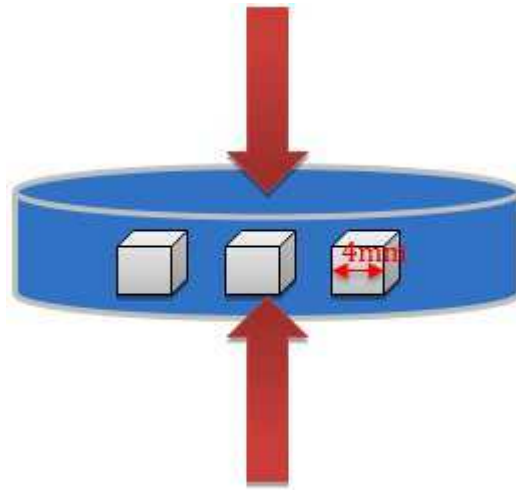


**Fig. 1** A schematic image showing the specimens size and the loading direction of compression test

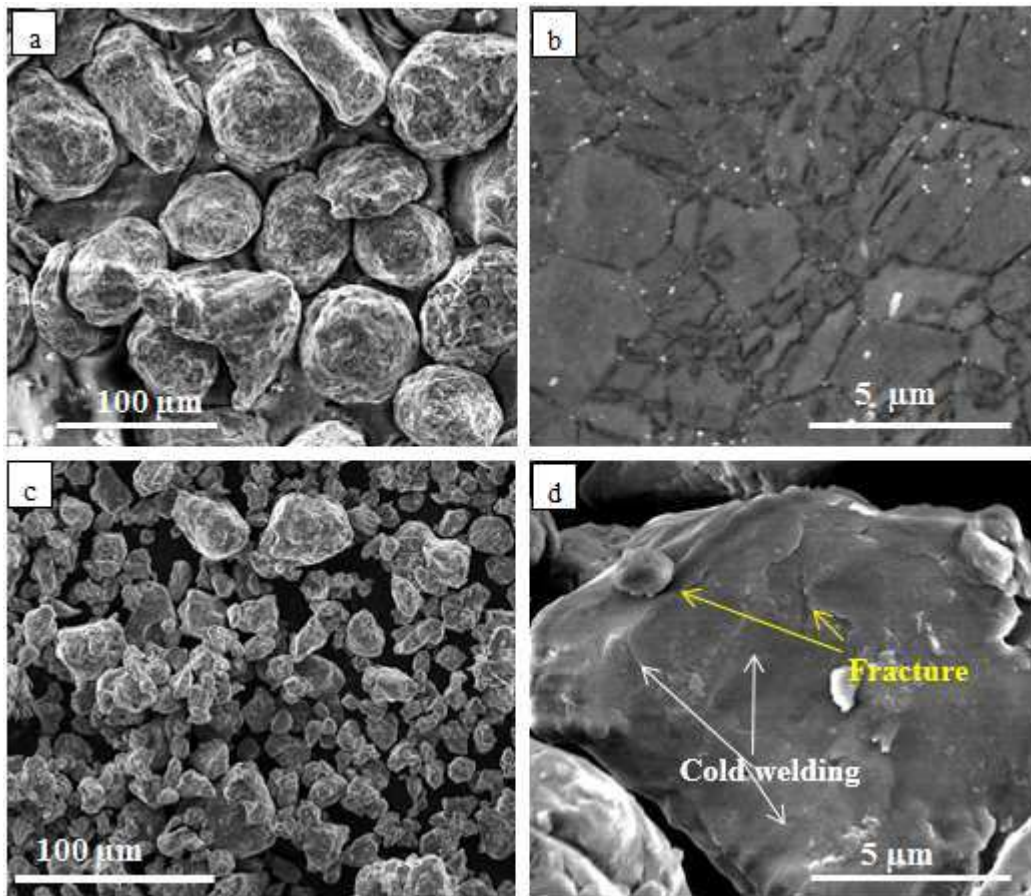


**Fig. 2** Typical SEM images showing (a) the morphology of as-received AZ31 powder, (b) internal grains of as-received AZ31 powder, (c) the morphology of cryomilled powder and (d) the signs of cold welding and fracture during cryomilling

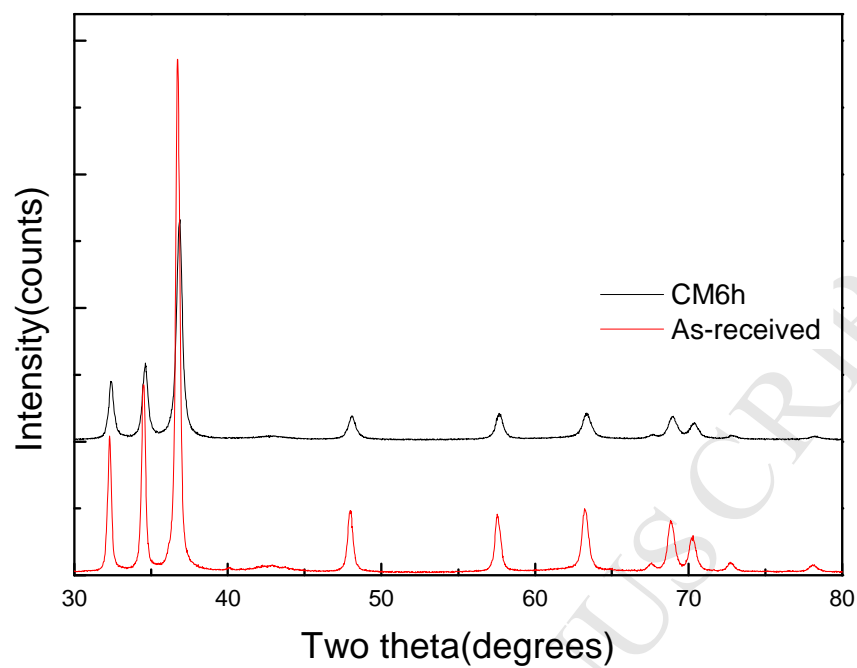


**Fig. 3** The XRD patterns of as-received and CM6h powders

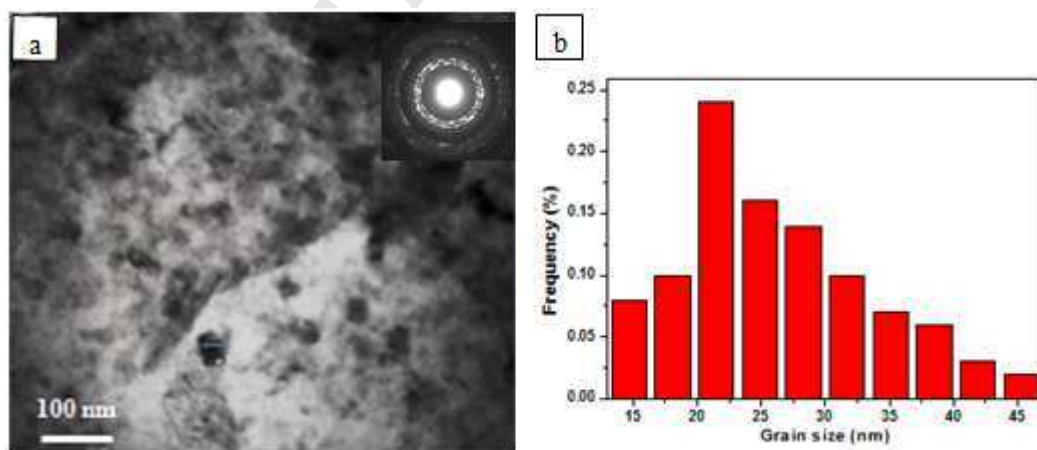


**Fig. 4** (a) Bright field TEM micrograph and selected area diffraction pattern of CM6h powder and (b) corresponding grain size distributions

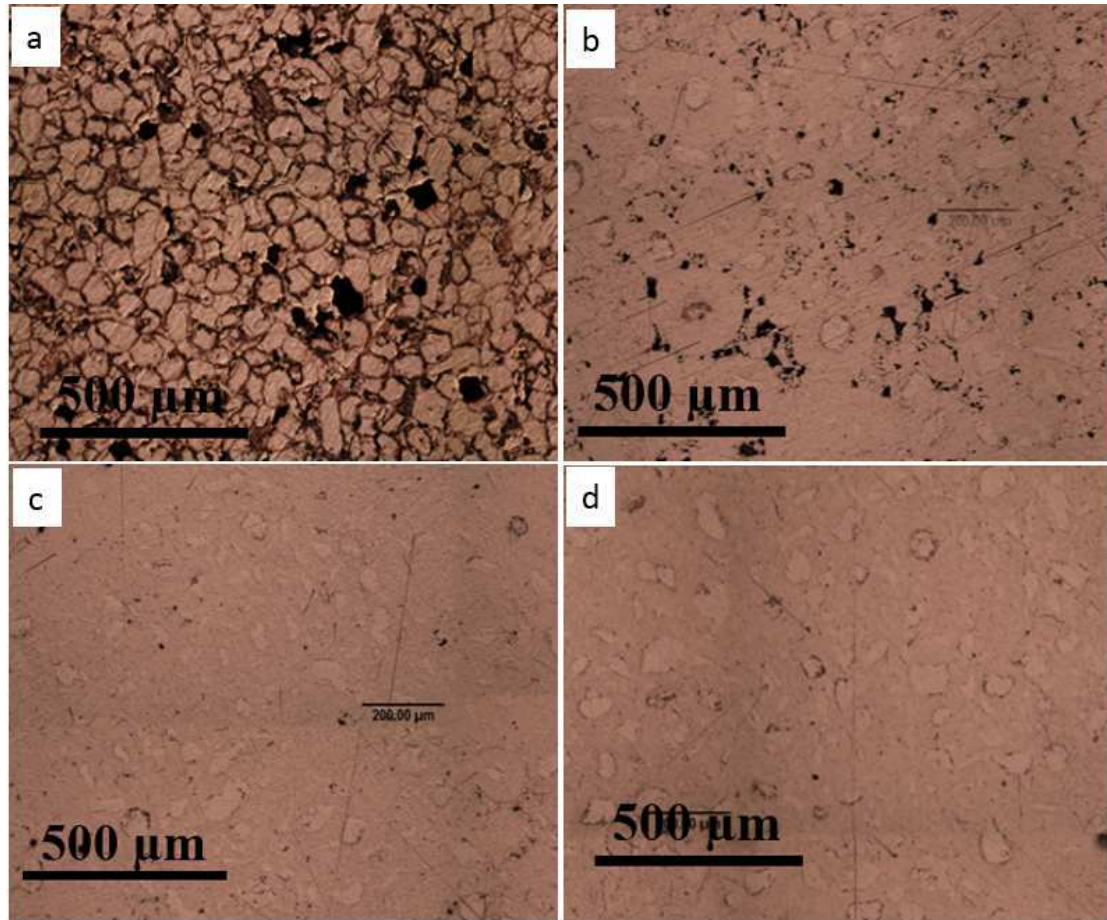


**Fig. 5** Typical optical microscope images of samples (a) AR400, (b) CM350, (c) CM400 and (d) CM450

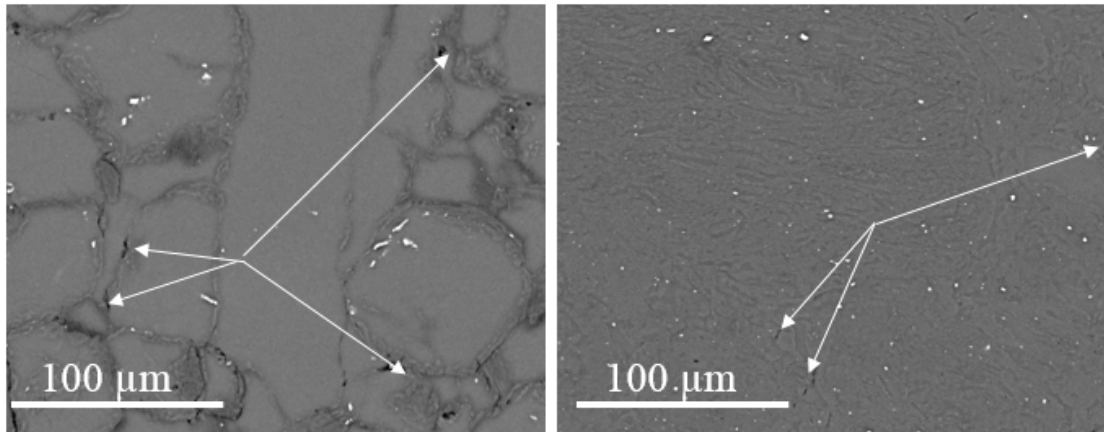


**Fig. 6** Back scattered electron SEM images of bulk (a) AR400 (b) CM400 sample

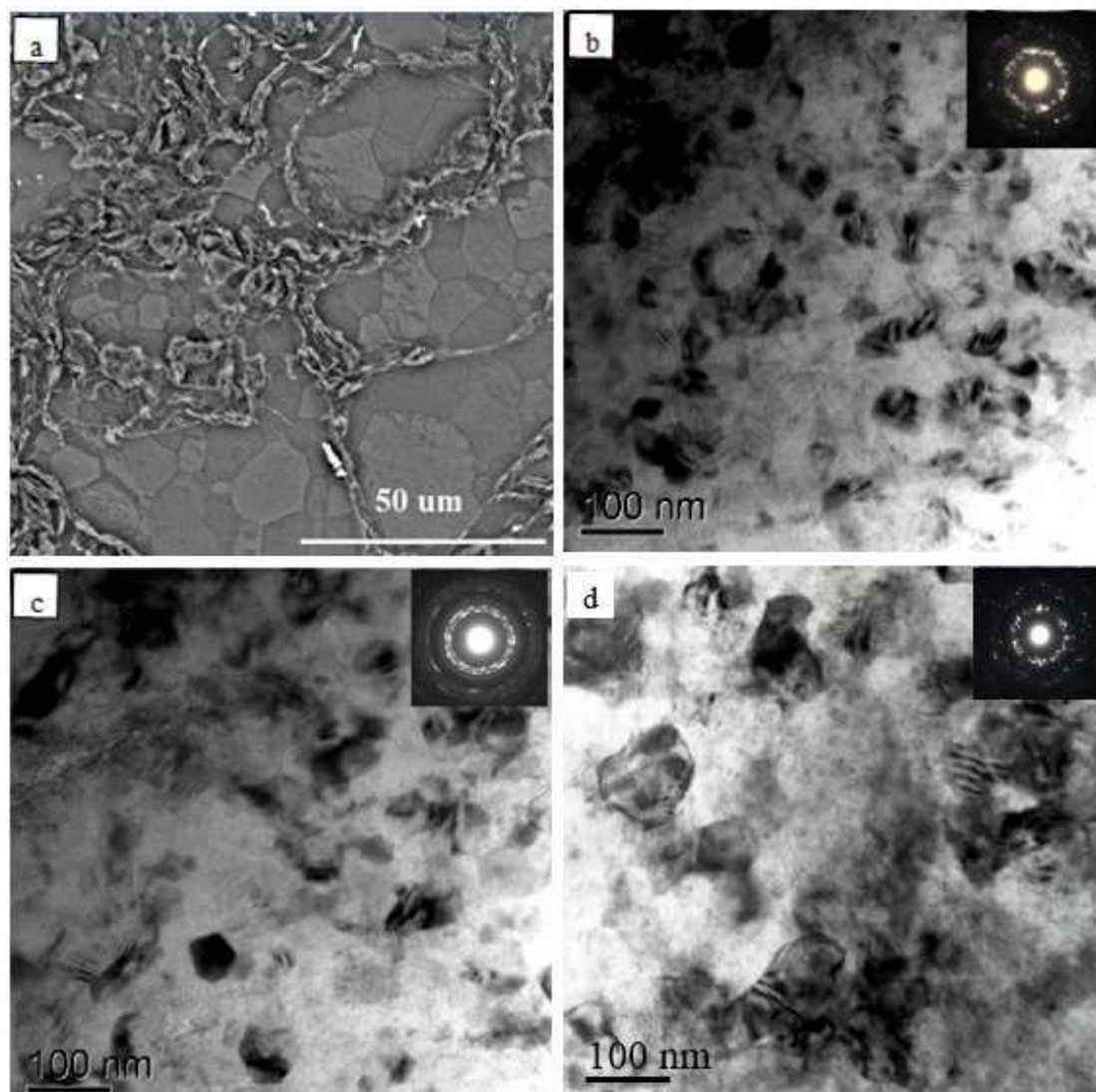


**Fig. 7** (a) Typical secondary electron SEM image of sample AR400 and typical bright field TEM images (with insert selected area diffraction patterns) of (b) CM350, (c) CM400 and (d) CM450

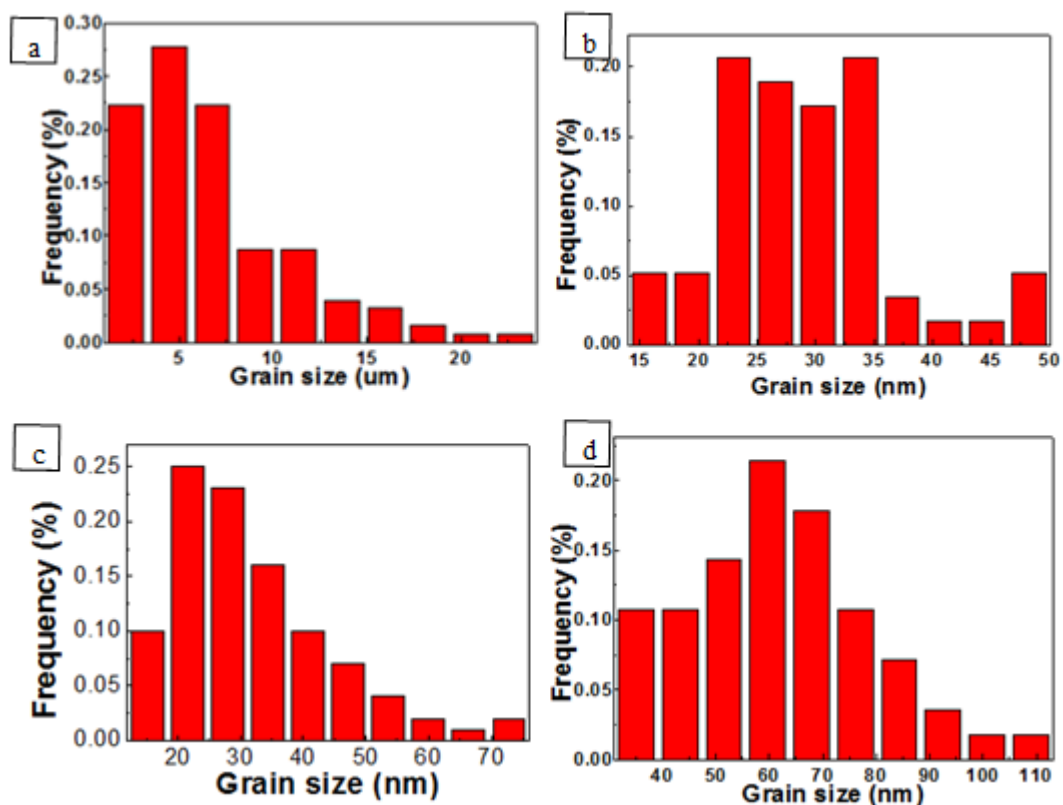


**Fig. 8** Grain size distributions of (a) AR400, (b) CM350, (c) CM400 and (d) CM450.

The AR400 was measured by SEM measurements, while the CM350, CM400 and CM450 were measured by TEM

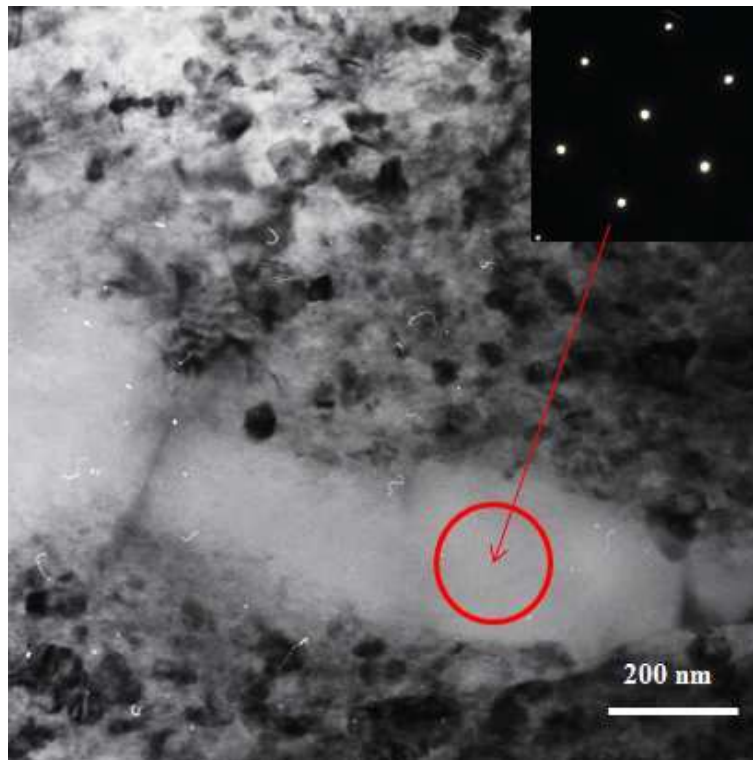


**Fig. 9** TEM image of sample CM400 showing a bimodal microstructure

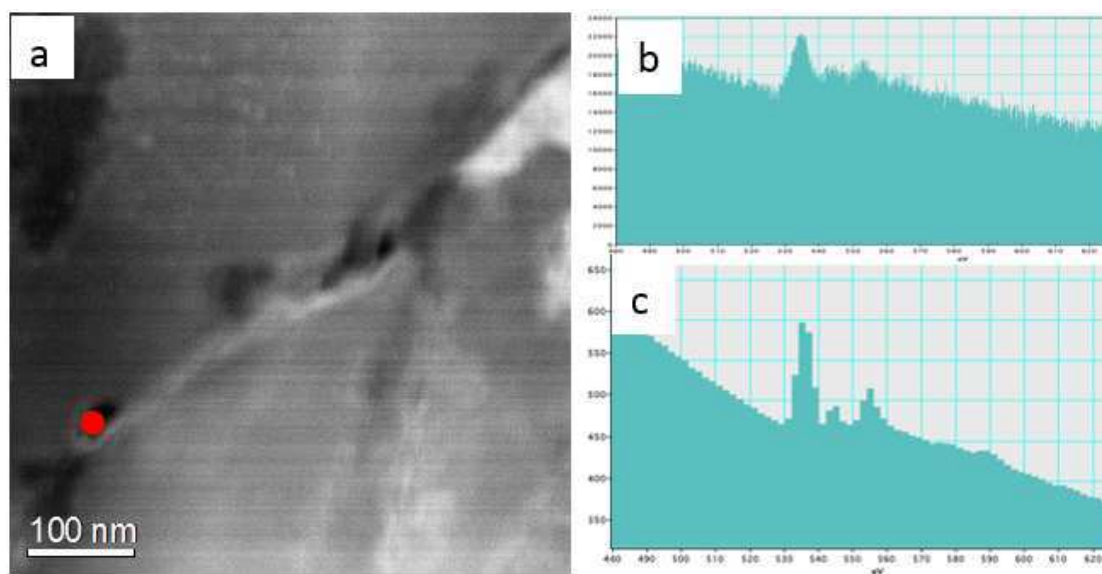


**Fig. 10** (a) High angle annular dark field (HAADF) image of bulk CM400 showing particles at a grain boundary, (b) Electron energy loss spectroscopy (EELS) spectrum collected from the red spot, showing the presence of oxygen and (c) a reference spectrum of MgO

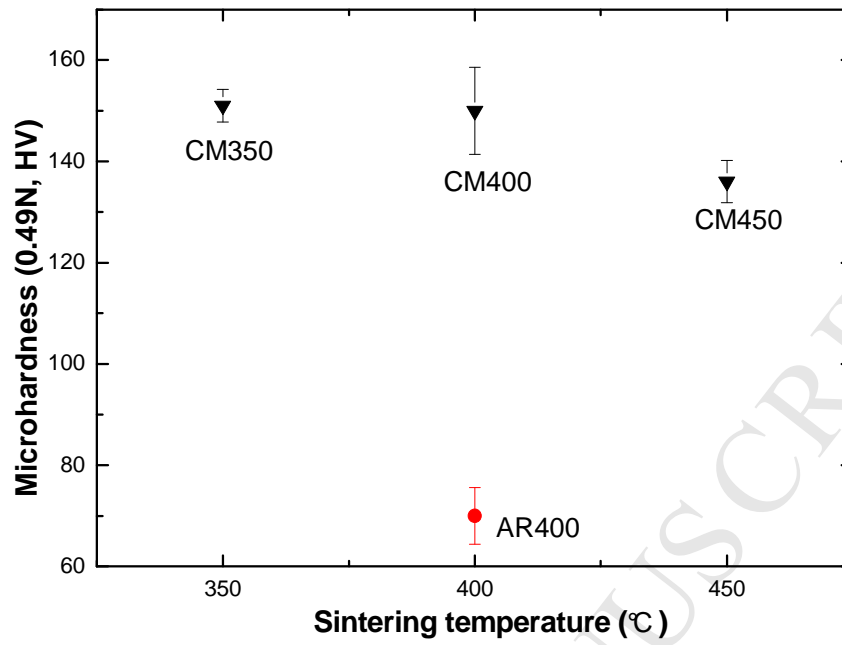


**Fig. 11** Micro hardness results of bulk samples produced by SPS from 350 °C to 450 °C

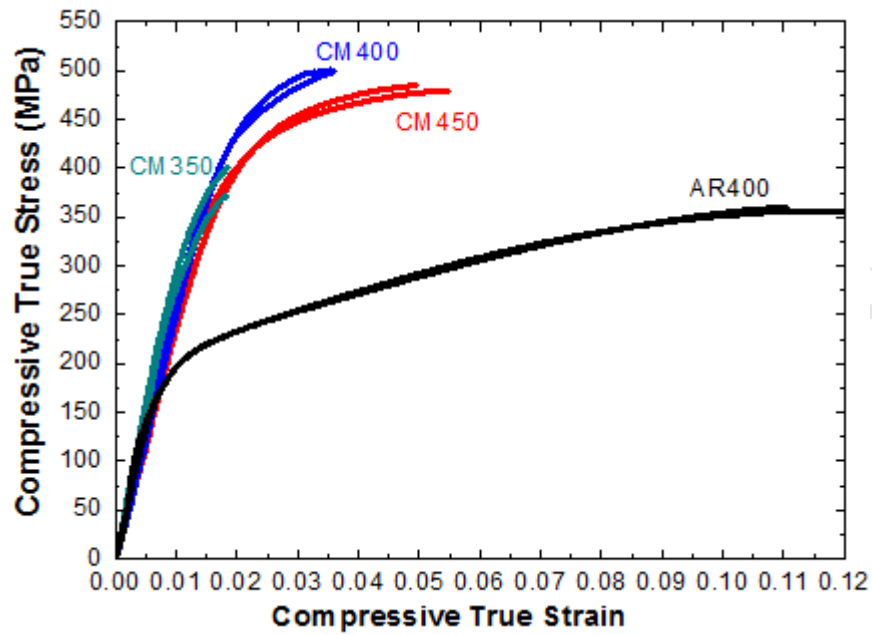


Fig. 12 Room temperature true stress-strain curves for bulk as-received and cryomilled samples

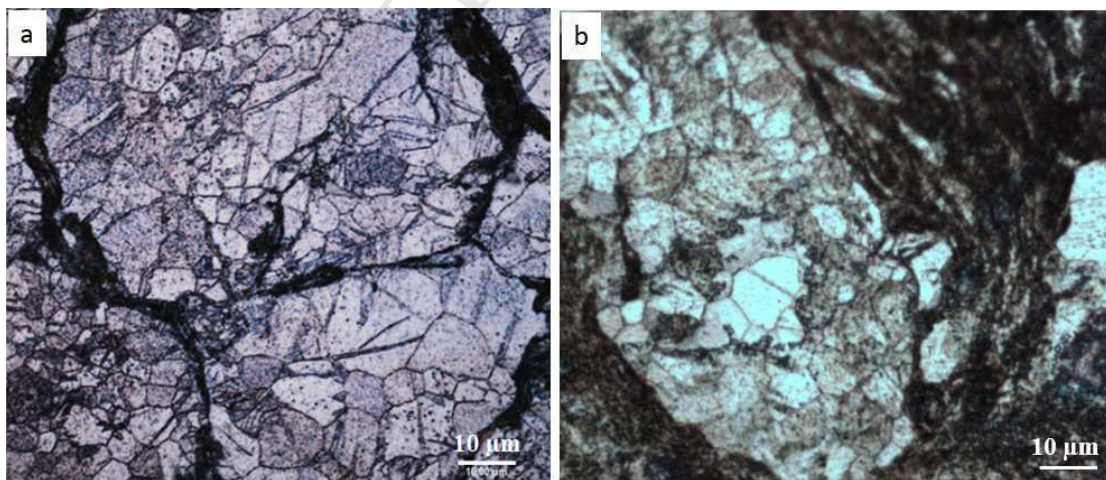


Fig. 13 Typical optical microscopy images of bulk samples (a) AR400 and (b) coarse grain area of CM400 after compression tests

**Highlights:**

1. Exceptionally high strength nanocrystalline AZ31 produced by cryomilling and SPS.
2. A mean grain size of 45nm obtained by 6h cryomill and SPS at 400°C.
3. The optimum conditions gave a yield of 401 MPa and ultimate strength of 500 MPa.
4. High strength attributed grain refinement and oxide dispersion hardening.